Journal of Nuclear Medicine, published on April 27, 2017 as doi:10.2967/jnumed.117.189514

Studies of a Next Generation Silicon-Photomultiplier-Based Time-of-Flight PET/CT System

David F.C. Hsu*[1,2], Ezgi Ilan[3,4], William T. Peterson[5], Jorge Uribe[5], Mark Lubberink[3,4], and Craig S. Levin**[1,2,6,7]

[1]Electrical Engineering, Stanford University, Stanford CA, USA
[2]Radiology, Stanford University, Stanford CA, USA
[3]Nuclear Medicine & PET, Department of Surgical Sciences, Uppsala University, Sweden
[4]Medical Physics, Uppsala University Hospital, Sweden
[5]GE Healthcare, Waukesha WI, USA
[6]Physics, Stanford University, Stanford CA, USA
[7]Bioengineering, Stanford University, Stanford CA, USA

**Corresponding author: Craig S. Levin
300 Pasteur Drive
Alway Building, Room M001
Stanford, CA 94305-5128
Phone: 650-736-7211
Fax: 650-724-1499
Email: cslevin@stanford.edu

*First author: David F.C. Hsu
(address same as above)
Phone: 217-819-1311
Fax: 650-724-1499
Email: fcdh@stanford.edu
David F.C. Hsu is currently a Ph.D student at Stanford University.

Word count: 5420

Financial support disclosure: Dr. Levin is currently participating in a sponsored research agreement with GE Healthcare on an un-related topic.

Working Title: Studies of a SiPM-based TOF PETCT System

ABSTRACT

This article presents system performance studies of the Discovery MI PET/CT system, a new time-of-flight (TOF) system based on silicon photomultipliers. System performance and clinical imaging comparisons were made between this next-generation system and other commercially available PET/CT and PET/MR systems, as well as between different reconstruction algorithms.

Methods Spatial resolution, sensitivity, NECR, scatter fraction, count rate accuracy, and image quality were characterized with the NEMA NU-2 2012 standards. Energy and coincidence time resolution were measured. Tests were conducted independently and results were averaged on two Discovery MI scanners installed at Stanford and Uppsala University Hospitals. Back-to-back patient scans were also performed between the Discovery MI PET/CT, Discovery 690 PET/CT, and SIGNA PET/MR systems. Clinical images were reconstructed with both ordered-subset expectation maximization (OSEM) and the "Q.Clear" reconstruction algorithms, and examined qualitatively.

Results The averaged full-width half max (FWHM) of the radial/tangential/axial spatial resolution reconstructed with FBP at 1, 10, and 20 cm from the system center are, respectively, 4.10/4.19/4.48 mm, 5.47/4.49/6.01 mm, and 7.53/4.90/6.10 mm. The averaged sensitivity is 13.7 cps/kBq at the center of the FOV. Averaged peak noise equivalent count rate is 193.4 kcps at 21.9 kBq/mL with a scatter fraction of 40.6%. The averaged contrast recovery coefficients for the image quality phantom are 53.7/64.0/73.1/82.7/86.8/90.7 for the 10/13/17/22/28/37 mm diameter spheres. The average photopeak energy resolution is 9.40% FWHM and the average coincidence time resolution is 375.4 ps FWHM. Clinical image comparisons between the PET/CT systems demonstrate the high quality of the Discovery MI system. Comparisons between the Discovery MI and SIGNA systems show similar spatial resolution and overall imaging performance. Lastly, results indicate significant image quality and contrast-to-noise performance enhancement for the "Q.Clear" reconstruction algorithm when compared to OSEM.

Conclusion Excellent performance was achieved with the new Discovery MI system, including 375 ps FWHM coincidence time resolution and sensitivity of 14 cps/kBq. Comparisons between different image

reconstruction algorithms and other multimodal SiPM and non-SiPM-based PET detector system designs indicate substantial performance enhancements are possible with this next-generation system.

Keywords PET/CT, NEMA, Characterization, Instrumentation, Image Reconstruction

INTRODUCTION

Positron emission tomography (PET) is a standard-of-care for cancer management, and has been integrated with computed tomography (PET/CT) and magnetic resonance imaging (PET/MR). PET/CT is commonly indicated for use in differentiating benign/malign tumors, staging cancer patients, and planning for radiation therapy (*1*). Improvements in system performance such as photon sensitivity, time resolution, and spatial resolution are expected to enhance diagnostic performance in lesion detection, low-dose patient imaging, and individualized treatment planning and evaluation (*2*). Many recent commercial PET-based systems have been evaluated using the National Electrical Manufacturers Association (NEMA) NU-2 standards, as reported in (*3–15*).

This paper reports on studies performed with the new Discovery MI PET/CT system produced by GE Healthcare (*16*), with the 4-ring PET configuration. The Discovery MI system combines 64 or 128-slice CT with a 3 or 4-ring PET system providing 15 or 20 cm of axial field-of-view (FOV) (*16*). Each PET ring employs 136 detector blocks, each of which comprise a 4x9 array of Lutetium-Yttrium Oxyorthosilicate crystals coupled to a 3x6 array of silicon photomultipliers (SiPMs) with Anger multiplexing for crystal identification. A closed-loop water cooling system, with real-time local temperature measurement and SiPM gain adjustment capabilities, is used to keep the SiPM arrays at a stable temperature of around 19°C in a similar manner as reported in Levin et. al (*17*). The crystal elements used in the system are 3.95 mm (transaxial) x 5.3 mm (axial) x 25 mm (length), while each Hamamatsu SiPM array has 2 x 3 pixels with an active area of 4 mm x 6 mm. A similar detector system design was employed in the SIGNA PET/MR system, and achieved a coincidence time resolution of sub-400 ps FWHM making it capable of advanced TOF performance (*17*).

MATERIALS AND METHODS

NEMA NU-2 2012 testing was performed independently on Discovery MI scanners installed at both Stanford and Uppsala University Hospitals. Prior to NEMA testing at both sites, a well counter calibration scan was performed with ^{18}F-Fluorodeoxyglucose (FDG) in an uniform cylindrical phantom. Unless otherwise specified, the testing protocol followed the NEMA NU-2 2012 standards exactly, with results from both institutions reported separately and not averaged together. Detailed procedures of each test can be found in the NEMA NU-2 2012 standards publication (*18*).

Due to interesting technology themes associated with this next-generation system, such as the use of SiPMs instead of photomultiplier tubes, the same detector technology used in both PET/CT and PET/MR systems, sub-400 ps coincidence time resolution, and the new generation of image reconstruction algorithms available, we have also added unique comparisons between different image reconstruction algorithms and other SiPM and non-SiPM-based PET/CT and PET/MR detector system designs to this paper. For clarity, Table 1 is provided as a reference for the different reconstruction-related acronyms that are used in the paper.

Spatial Resolution

Spatial resolution was measured by creating ^{18}F-FDG point sources using capillary tubes, and suspending them at radial offsets of 1/10/20 cm and axial offsets of 0/7.5 cm from the center of the FOV (CFOV). Data were collected for 1 minute at each position. The FWHM and full-width tenth max (FWTM) of the point sources were quantified at all locations, using the NEMA-specified FBP algorithm, as well as the VPHD algorithm.

Sensitivity

Plastic tubing (70 cm length, 1 mm inner diameter) was filled with an averaged calibrated activity of approximately 20 MBq of ^{18}F-FDG at both institutions, allowed to decay 250 minutes to reach an activity that generates less than 5% randoms, and fixed at both the CFOV and a vertical

radial offset of 10 cm using positioning scans and a positioning apparatus. One minute scans were taken with 5 sets of aluminum sleeves with increasing thicknesses that ensure complete annihilation of all generated positrons. NEMA sensitivity calculations were performed after randoms subtraction to ensure trues-only datasets.

Count Rate Statistics

The patient table was moved to its lowest setting, and the NEMA scatter phantom was propped up to the CFOV on stacks of low-density material placed outside the FOV. A line source (70 cm length, 3.2 mm inner diameter) was filled with a calibrated activity of roughly 817 MBq of ^{18}F-FDG and inserted into the NEMA scatter phantom. Twenty-four frames of data were taken, with the first 17 frames taken with 15 minute acquisitions, and the last 7 frames taken with 25 minute acquisitions followed by 25 minute delays (i.e. at 50 minute intervals). NEMA specifications were used to derive the trues, randoms, scatter, and noise-equivalent count rate (NECR) from the prompts dataset in each frame. Randoms were estimated using singles rates.

Accuracy of Correction

The count rate accuracy of the system, which compares the measured activity to the expected activity and is dependent on the system corrections used, was found from a linear fit of the activity concentrations measured below peak NECR. In addition to attenuation and scatter correction, randoms and deadtime corrections were performed using singles-based randoms subtraction and pileup correction, respectively. Reconstructed image matrix dimensions were 128 x 128 with a pixel size of 1.41 mm x 1.41 mm.

Image Quality

The NEMA image quality phantom background region and the 10/13/17/22 mm diameter spheres were filled, respectively, with ^{18}F-FDG activity concentrations of 4.7 kBq/mL and 18.8 kBq/mL at Stanford, as well as 5.1 kBq/mL

and 20.4 kBq/mL at Uppsala, yielding a 4:1 sphere to background concentration ratio. The 28/37 mm diameter spheres were filled with non-radioactive water. The scatter line source used to measure NEMA count rate statistics was filled with roughly 118 MBq of ^{18}F-FDG and threaded through the body phantom. For reproducibility, three separate acquisitions of the image quality phantom were taken with decay-adjusted acquisition times of 271/279/282 seconds, consistent with a 151 mm axial step for each bed position, and reconstructed with the standard GE clinical VPFX reconstruction algorithm and the recently-released Q.Clear reconstruction algorithm (*19*) (beta = 50, yielding similar noise levels as VPFX). The average and standard deviation of the contrast recovery (CR) and background variability were quantified over the 3 sets of data replicates. The following corrections were applied to the data: randoms, scatter, CT-based attenuation, dead time, and normalization. Reconstructed image matrix dimensions were 384 x 384 x 71, with pixel size of 1.042 mm x 1.042 mm and slice thickness of 2.790 mm.

Energy and Timing Resolution

A line source 70 cm in length was filled with 12 MBq of ^{18}F-FDG solution and suspended at the CFOV in the axial direction inside the smallest aluminum sleeve used in the NEMA sensitivity measurement. 400 million coincident counts were taken to acquire the timing and energy spectra. The timing resolution FWHM was measured based on a 3 point fit of the peak for each crystal pair's timing spectra after randoms were removed. For the energy resolution, the energy spectra were smoothed with a boxcar filter, and the percentage FWHM per channel was measured. The system timing and energy resolutions were quantified by averaging the values from all the detector crystals and channels in the system.

Clinical Imaging Comparison with Discovery 690 PET/CT System

To study potential benefits of SiPM technology, we compared performance with a photomultiplier-tube-based PET/CT system at Stanford University Hospital. For the purpose of restaging and metastatic evaluation, a

patient with a clinical history of melanoma was injected with 298 MBq of ^{18}F-FDG, and a 33 minute total body scan was first taken 96 minutes post-injection on the Discovery 690 PET/CT system. At roughly 130 minutes post-injection, another total body scan of 33 minutes duration was taken on the Discovery MI PET/CT system. The image corrections that were applied include singles-estimate randoms correction, CT-based scatter and attenuation correction, and dead time correction. For both PET/CT systems, VPFX reconstruction was performed with 3 iterations, 16 subsets, and a 5 mm post filter. In addition, Q.Clear reconstruction was performed with a beta value of 350 for both systems, which was chosen to match the noise level in the VPFX reconstructions.

Clinical Imaging Comparison with SIGNA PET/MR System

Because the same basic SiPM-based detector design was incorporated in both the Discovery MI PET/CT and SIGNA PET/MR systems, we are in the unique position to compare the PET performance in CT vs. MR environments. A female patient with neuroendocrine tumors (102 kg, age 54) was scanned with ^{68}Ga-DOTATOC on the Discovery MI and the SIGNA systems over two consecutive days at Uppsala University Hospital. On the Discovery MI system, the scan began 72 mins after the injection of 181 MBq of ^{68}Ga-DOTATOC, with 2 mins/bed position. On the SIGNA system, the scan began 69 mins after the injection of 148 MBq of ^{68}Ga-DOTATOC, with 3 mins/bed position. Image reconstruction with the VPFX-S algorithm was performed on both systems, with 3 iterations, 16 subsets, and a 5 mm post filter. In addition, Q.Clear reconstruction with a beta value of 350 was also performed on the Discovery MI scan. Attenuation correction was performed using a standard two-point Dixon MR sequence.

RESULTS

Spatial Resolution

Spatial resolution results are shown in Table 2, for both FBP and VPHD reconstruction algorithms.

Sensitivity

The sensitivity at the CFOV is 14.0 cps/kBq at Stanford and 13.4 cps/kBq at Uppsala. The sensitivity at a radial offset of 10 cm is 13.8 cps/kBq at Stanford and 13.1 cps/kBq at Uppsala. The slice sensitivity profile at the CFOV is shown in Figure 1a, while Figure 1b shows the extrapolation process to remove the attenuation from the aluminum tubes in order to obtain attenuation-free sensitivity numbers.

Count Rate Statistics

Figure 2a shows the trues, randoms, scatters, NECR, and total event rate as a function of activity. Figure 2b shows the system scatter fraction as a function of activity. Table 3 summarizes important count rate metrics measured at both Stanford and Uppsala University.

Accuracy of Correction

The average count rate error at both institutions, defined by the percentage deviation from the expected activity, is shown in Figure 3 as a function of the activity concentration in the line source. The error bars indicate the maximum positive and negative slice deviations from the average error at each activity. The maximum deviation from expected activity at Uppsala is 3.86% at an activity concentration of 1.19 kBq/mL, while at Stanford it is 2.43% at an activity of 35.44 kBq/mL.

Image Quality

The image CR and background variability (BV) of the image quality phantom are shown in Table 4 and represented visually in Figure 4. The average lung error (ΔC_{lung}) for the VPFX reconstruction is 4.4%±0.1% at Stanford and 5.3%±0.0% at Uppsala, while for the Q.Clear reconstructions it is 2.5%±0.1% at Stanford and 3.3%±0.1% for Uppsala. The reconstructed transverse and coronal images from the NEMA image quality phantom are shown in Figure 5, showing the better noise and CR performance of the Q.Clear reconstruction.

Energy and Timing Resolution

The average system photopeak energy resolution is 9.44%±0.07% FWHM at Stanford and 9.35%±0.05% FWHM at Uppsala. The average system coincidence time resolution is 374.1±2.6 ps FWHM at Stanford and 376.7±2.7 ps FWHM at Uppsala.

Clinical Imaging Comparison with Discovery 690 PET/CT System

Three different sets of PET/CT patient images from both the Discovery 690 and Discovery MI systems are shown in Figure 6, corresponding to maximum-intensity projection coronal images that show lesions on different coronal slices, PET axial slices, and fused PET/CT axial slice images. Because the two PET/CT systems have different axial slice thicknesses, the images displayed were carefully chosen to ensure the best alignment possible.

Clinical Imaging Comparison with SIGNA PET/MR System

In Figure 7, coronal slice and coronal maximum-intensity projection images are shown for the Discovery MI and SIGNA systems with the VPFX-S and Q.Clear reconstructions. The alignment of the slices and the image

intensity scale between the systems was chosen to be as close as possible between the two systems.

DISCUSSION

Inter-System Variances

Inter-system variations from the system manufacturing process may explain general trends in the variations between the 2 systems, such as the Stanford system's better count rate performance and worse CR performance. However, differences during the phantom filling process might also have caused some variations in the results. Imperfect filling of the 17 mm sphere at Stanford could explain its lower CR numbers, while differences in capillary tube axial confinement could explain differences in the axial spatial resolution. The lower sensitivity measured at Uppsala may also be caused by variations in activity calibrations used in the dose calibrator.

Performance Measurement Observations

Due to this system's high photon sensitivity and the low recommended clinical dosage, the NECR testing did not reach the system's peak trues count rate and activity. The amount of activity required would be so high as to require sweeping a large non-clinically relevant portion of the NECR curve. Similarly, the measured maximum relative count rate error at both institutions occur at activity levels that are not clinically relevant, while it is less than 3% across both institutions when restricted to clinically relevant activity levels. A low relative count rate error is clinically important for accurate lesion quantization, post-treatment follow up scans, and longitudinal studies. The background activity concentration used in the image quality phantom at Stanford was 0.6 kBq/mL lower than the NEMA specifications. This leads to a more conservative CR measurement due to a lower number of acquired counts, and could explain the 8% lower measured CR observed for the smaller spheres observed in Stanford's system compared to Uppsala's. A reduction in the system axial FOV from 20 cm to 15 cm (3-ring configuration) would result in a reduced sensitivity of 7.5 kcps/MBq and peak NECR

of 100 kcps at 20.6 kBq/mL (*16*). It should also be noted that the measured energy and timing resolution can be improved by using lower activity levels.

Clinical System Comparisons

A visual observation of Figure 6 shows several lesions, shown by the blue arrows, that are only visible in the Discovery MI image regardless of the reconstruction method used. This is likely due to the Discovery MI's improved sensitivity, NECR, timing resolution, and CR of small lesions when compared to the 690 as shown in Table 5. It must be noted, however, that direct comparisons cannot be made due to the different tracer uptake time and patient alignment of the two acquisitions. Comparing the Q.Clear reconstruction versus the more traditional VPFX reconstruction, the intensity of lesion uptake is clearly higher in the Q.Clear images, with better defined lesion boundaries. This improvement can help in surgery and radiotherapy planning, or tumor segmentation for quantitative studies on treatment effectiveness.

Similarly to the comparisons with the Discovery 690, direct comparisons cannot be made between the Discovery MI and SIGNA systems because the patient was scanned on two consecutive days, with slightly different amounts of activity and scan time per bed position. However, it is clear from Figure 7 that, visually speaking, the lesion identification capability and spatial resolutions of the Discovery MI and SIGNA systems are similar, which is not surprising since they utilize very similar block detector architectures (*17*). There are also no significant visual differences for lesion visualization near the center of the body between CT-based and MR-based attenuation correction of the two systems. The VPFX-S reconstructed coronal slice image comparisons show better noise performance in the Discovery MI system compared to the SIGNA system, making lesion identification easier. Similar to the discussion in the previous paragraph, the use of Q.Clear reconstruction instead of OSEM-based reconstruction dramatically suppresses background noise while having minimal effects on lesion intensity.

Comparisons with other Multimodal Systems

Table 5 offers a comparison of published NEMA NU-2 measurements made on some of the newest commercial multimodal PET scanners that are offered by GE, Siemens, and Philips. For comparison purposes, the Discovery MI PET/CT performance metrics in this table are calculated from averaging the NEMA NU-2 results from Stanford and Uppsala. Of the listed systems, the GE Discovery MI, GE SIGNA, Siemens Biograph mCT Flow, and Philips Vereos systems were tested with the NEMA NU-2 2012 standards, while the rest were tested with the NEMA NU-2 2007 standards.

Comparisons between the NEMA NU-2 2007 and 2012 standards must take into account slight differences between the 2 specifications. For spatial resolution tests, the 2007 standard does not report radial offsets of 20 cm or separate radial and tangential resolutions at the CFOV, and it averages the resolutions of 2 sources at 10 cm radial offsets in orthogonal directions. For NECR tests, the 2007 standard does not allow shimming of the phantom, leading to larger table scatter contribution for systems with a large table height adjustment range. The count rate accuracy measured by the 2007 standard uses extrapolation over the lowest 3 measurement points instead of over all points below peak NECR, and it also does not require corrections to be performed on reconstructed images, which can be challenging for scatter models that vary with count rate. Most significantly, the image quality measured in the 2007 standards use acquisitions that are twice as long as the 2012 standards, leading to artificially favorable CR and BV values measured using the 2007 standards.

The spatial resolution testing results show that, taken as a whole over all three resolution directions and the different distances from the CFOV, the Discovery MI has comparable performance when compared against the systems in the table.

The Discovery MI has the highest sensitivity of all the PET/CT systems, although it is still lower than the PET/MR systems with longer PET axial FOVs and smaller transaxial FOVs. A high sensitivity allows nuclear medicine clinics to achieve better image SNR for a given image acquisition time, or to maintain the same image SNR while shortening acquisition times or reducing patient dose. This observation is reinforced with the count rate performance of the Discovery MI system.

Compared to the Discovery 690 system, the Discovery MI system has a peak NECR that is 39% higher, and a peak NEC activity concentration that is 24% lower. The higher peak NECR allows it to achieve the same image SNR with a 39% shorter scan time, and even more so when accounting for the improved timing resolution and associated TOF SNR gain of the Discovery MI system. The lower peak NEC activity concentration points to its viability as a low-dose imaging system.

The CR of the smaller spheres scanned by the Discovery MI is better than all the other commercially available systems in Table 5. Compared to the Discovery 690 PET/CT system, which has the next best CR performance, the CR of the Discovery MI is 22% better for the 10 mm sphere, 14% better for the 13 mm sphere, 12% better for the 17 mm sphere, and 11% better for the 22 mm sphere. This should lead to an improvement in the system's ability to detect, visualize, and quantify smaller lesions.

CONCLUSION

In conclusion, NEMA NU-2 2012 testing was performed on the new SiPM-based Discovery MI PET/CT systems at Stanford University and Uppsala University. The results point to improved diagnostic sensitivity of smaller sized lesions, and a wide range of promising applications of the Discovery MI from low-dose oncology studies to high-dose short lived isotope PET/CT imaging. In addition, comparisons made with other PET/CT and PET/MR systems demonstrate the substantial performance improvements possible with the new generation of SiPM-based TOF PET/CT systems.

ACKNOWLEDGEMENTS

The authors would like to acknowledge Adam Brown, Jakub Siennicki, and Tarik Cengiz from GE Healthcare, Monica Ranger and Vinh Nguyen from Stanford Healthcare, Dr. Fred Chin and the Radiochemistry group at Stanford, and Lars Lindsjö and Professor Anders Sundin from Uppsala University Hospital, for their valuable contributions in the data collection process for this publication.

REFERENCES

[1] Boellaard R, Delgado-Bolton R, Oyen WJG, et al. FDG PET/CT: EANM procedures guidelines for tumour imaging: version 2.0. *Eur J Nucl Med Mol I.* 2015;42:328-354.

[2] Ell PJ. The contribution of PET/CT to improved patient management. *Brit J Radiol.* 2006;79:32-36.

[3] De Ponti E, Morzenti S, Guerra L, et al. Performance measurements for the PET/CT Discovery-600 using NEMA NU 2-2007 standards. *Med Phys.* 2011;38:968–974.

[4] Bettinardi V, Presotto L, Rapisarda E, Picchio M, Gianolli L, Gilardi MC. Physical performance of the new hybrid PET/CT Discovery-690. *Med Phys.* 2011;38:5394–5411.

[5] Marti-Climent JM, Prieto E, Dominguez-Prado I, et al. Contribution of time of flight and point spread function modeling to the performance characteristics of the PET/CT Biograph mCT scanner. *Rev Esp Med Nucl.* 2013;32:13–21.

[6] Jakoby BW, Bercier Y, Conti M, Casey ME, Bendriem B, Townsend DW. Physical and clinical performance of the mCT time-of-flight PET/CT scanner. *Phys Med Biol.* 2011;56:2375–2389.

[7] Rausch I, Cal-González J, Dapra D, et al. Performance evaluation of the Biograph mCT Flow PET/CT system according to the NEMA NU2-2012 standard. *Eur J Nucl Med Mol I.* 2015;2:1–17.

[8] Kolthammer JA, Su KH, Grover A, Narayanan M, Jordan DW, Muzic RF. Performance evaluation of the Ingenuity TF PET/CT scanner with a focus on high count-rate conditions. *Phys Med Biol.* 2014;59:3843–3859.

[9] Surti S, Kuhn A, Werner ME, Perkins AE, Kolthammer J, Karp JS. Performance of Philips Gemini TF PET/CT scanner with special considerations for its time-of-flight imaging capabilities. *J Nucl Med.* 2007;48:471–480.

[10] Grogg KS, Toole T, Ouyang J, et al. National Electrical Manufacturers

Association and clinical evaluation of a novel brain PET/CT scanner. *J Nucl Med.* 2016;57:646–652.

[11] Akamatsu G, Uba K, Taniguchi T, et al. Impact of time-of-flight PET/CT with a large axial field of view for reducing whole-body acquisition time. *J Nucl Med Technol.* 2014;42:101–104.

[12] Grant AM, Deller TW, Khalighi MM, Maramraji SH, Delso G, Levin CS. NEMA NU 2-2012 performance studies for the SiPM-based ToF-PET component of the GE SIGNA PET/MR system. *Med Phys.* 2016;43:2334–2343.

[13] Karlberg AM, Sæther O, Eikenes L, Goa PE. Quantitative comparison of PET performance–Siemens Biograph mCT and mMR. *Eur J Nucl Med Mol I.* 2016;3:1–14.

[14] Delso G, Fürst S, Jakoby B, et al. Performance measurements of the Siemens mMR integrated whole-body PET/MR scanner. *J Nucl Med.* 2011;52:1914–1922.

[15] Teoh EJ, McGowan DR, Macpherson RE, Bradley KM, Gleeson FV. Phantom and clinical evaluation of the Bayesian penalized likelihood reconstruction algorithm Q.Clear on an LYSO PET/CT system. *J Nucl Med.* 2015;56:1447–1452.

[16] Levin CS, Peterson W, Ross S, Stearns C, Uribe J. PET performance as a function of axial field of view for a new silicon photomultiplier-based whole body TOF PET/CT system. *J Nucl Med Suppl.* 2016;2:200.

[17] Levin CS, Maramraji SH, Khalighi MM, Deller TW, Delso G, Jansen F. Design features and mutual compatibility studies of the time-of-flight PET capable GE SIGNA PET/MR system. *IEEE Trans Med Imaging.* 2016;35:1907-1914.

[18] National Electrical Manufacturers Association. *NEMA NU-2 2012: Performance Measurement of Positron Emission Tomographs.* 2013.

[19] Lantos J, Iagaru A, Levin CS. Scanner dependent noise properties of the Q.Clear PET image reconstruction tool *IEEE Nuc Sci Symp Med Imag Conf Rec.* 2015:1-3.

[20] Zhang J, Miller M, Knopp MV. Performance evaluation of digital

PET/CT: medical physics basis for the clinical applications. *Med Phys.* 2016;43:3399.

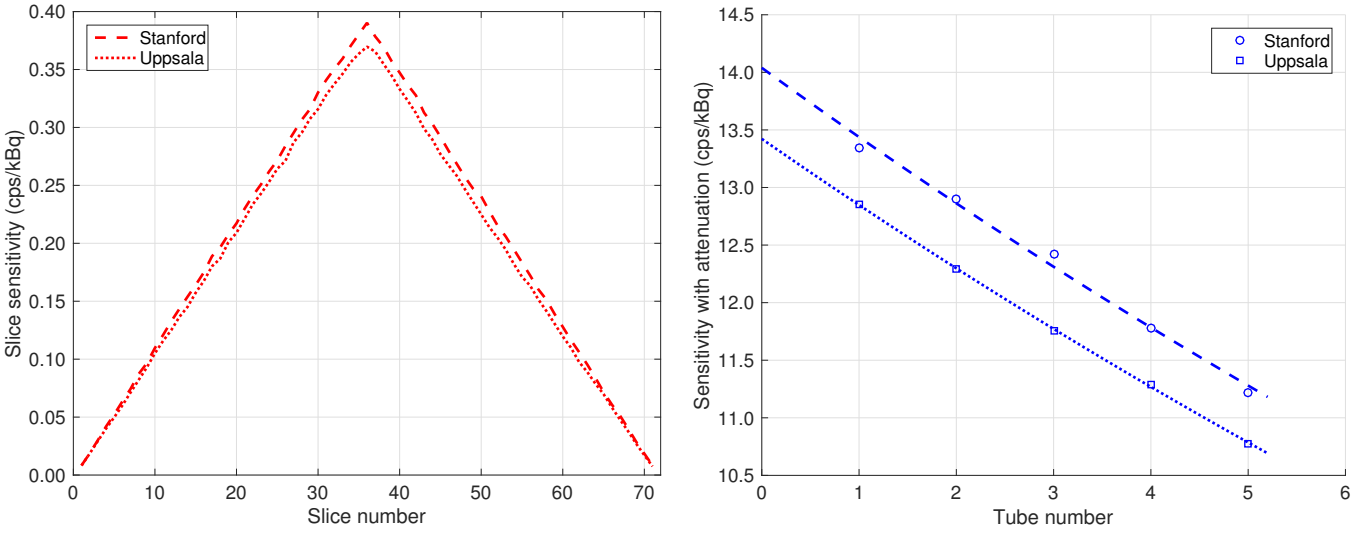

(a) Sensitivity of different axial slices.

(b) Sensitivity as a function of the number of attenuating aluminum sleeves.

Figure 1: NEMA sensitivity measurement results.

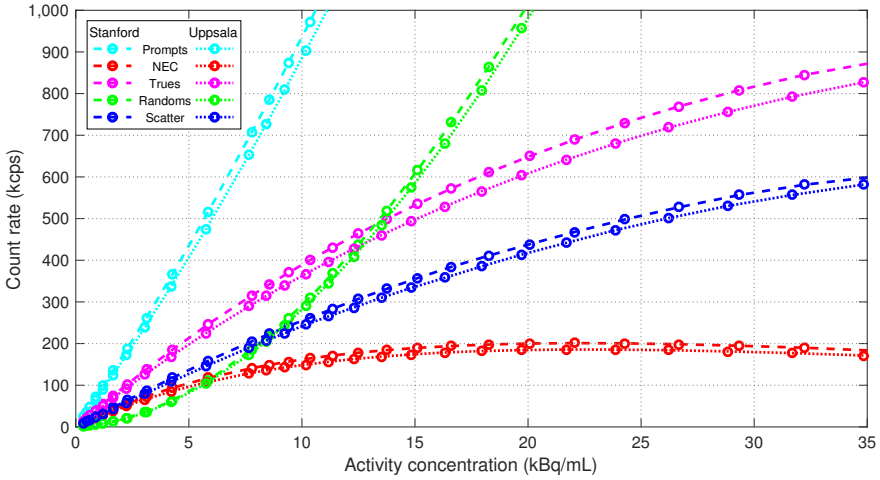

(a) Count rate vs. activity.

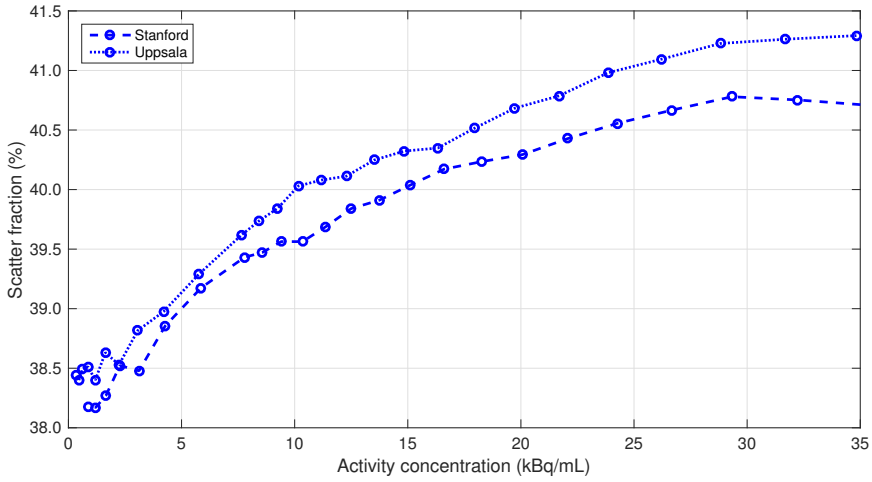

(b) Scatter fraction vs. activity.

Figure 2: NEMA count rate measurement results.

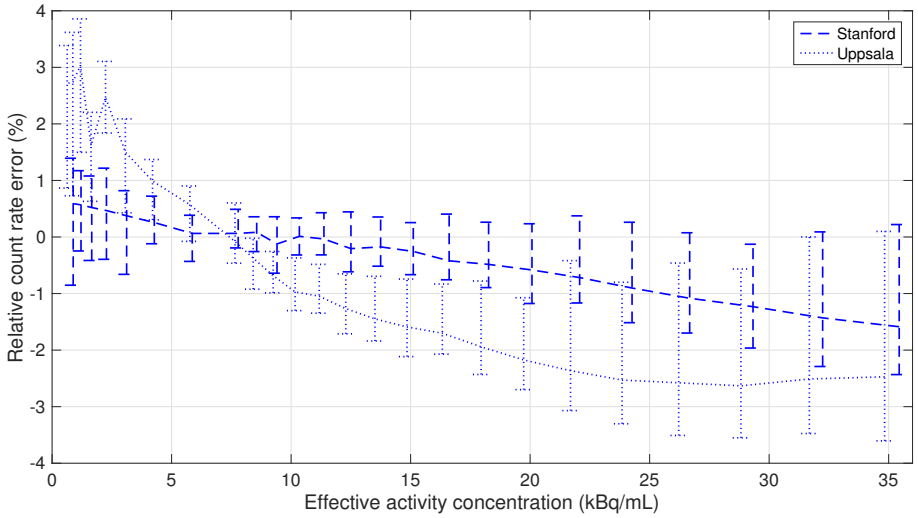

Figure 3: Count rate error measured as percent deviation from expected activity concentration. Error bars show the range of deviations from the expected activity level.

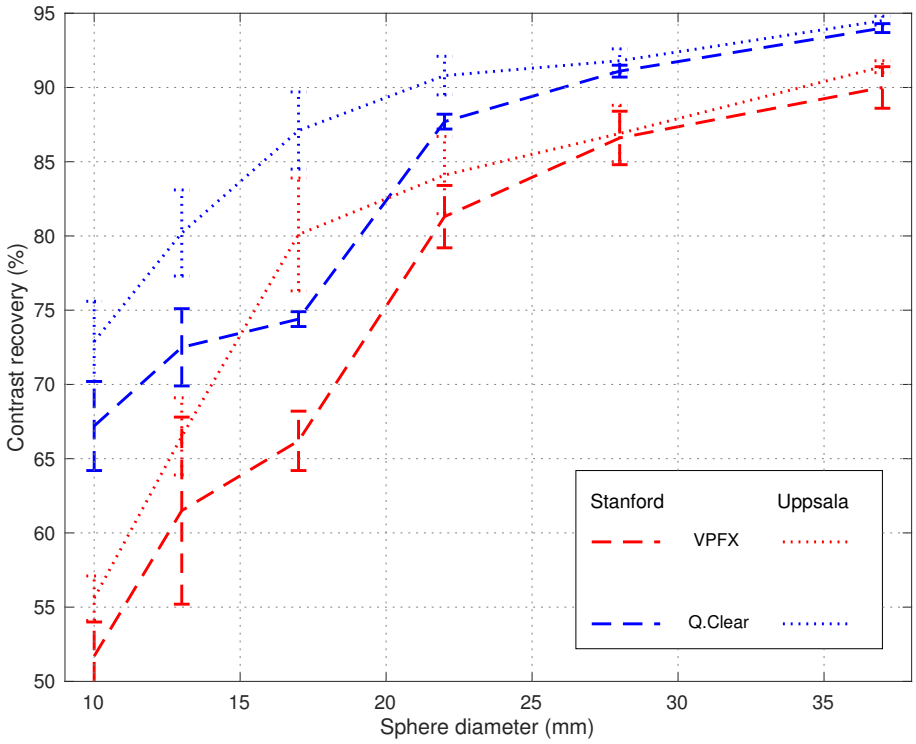

Figure 4: CR and BV values measured with the VPFX and Q.Clear reconstructions at Stanford and Uppsala.

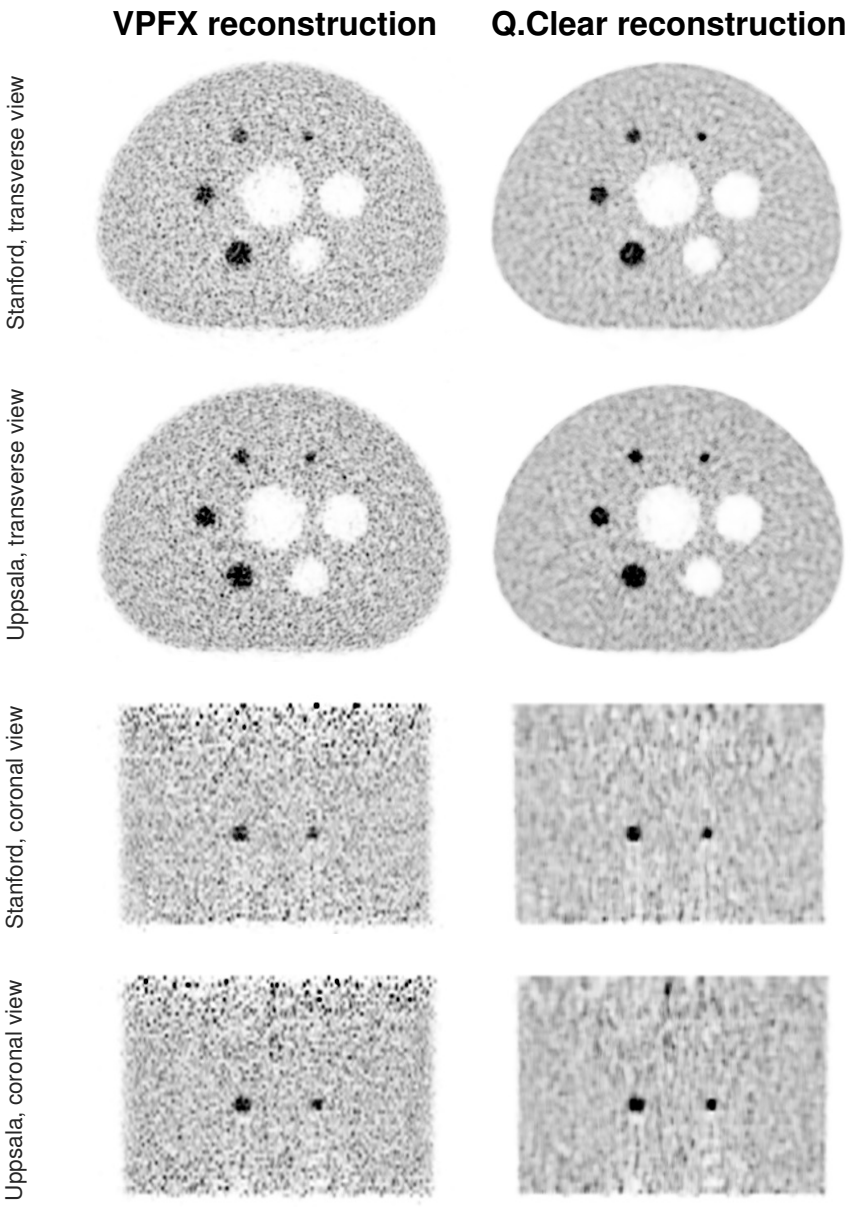

Figure 5: Image quality phantom images, reconstructed with the VPFX and Q.Clear reconstruction algorithms. Top: transverse slices through the center of all spheres. Bottom: coronal slices through the 10/13 mm spheres.

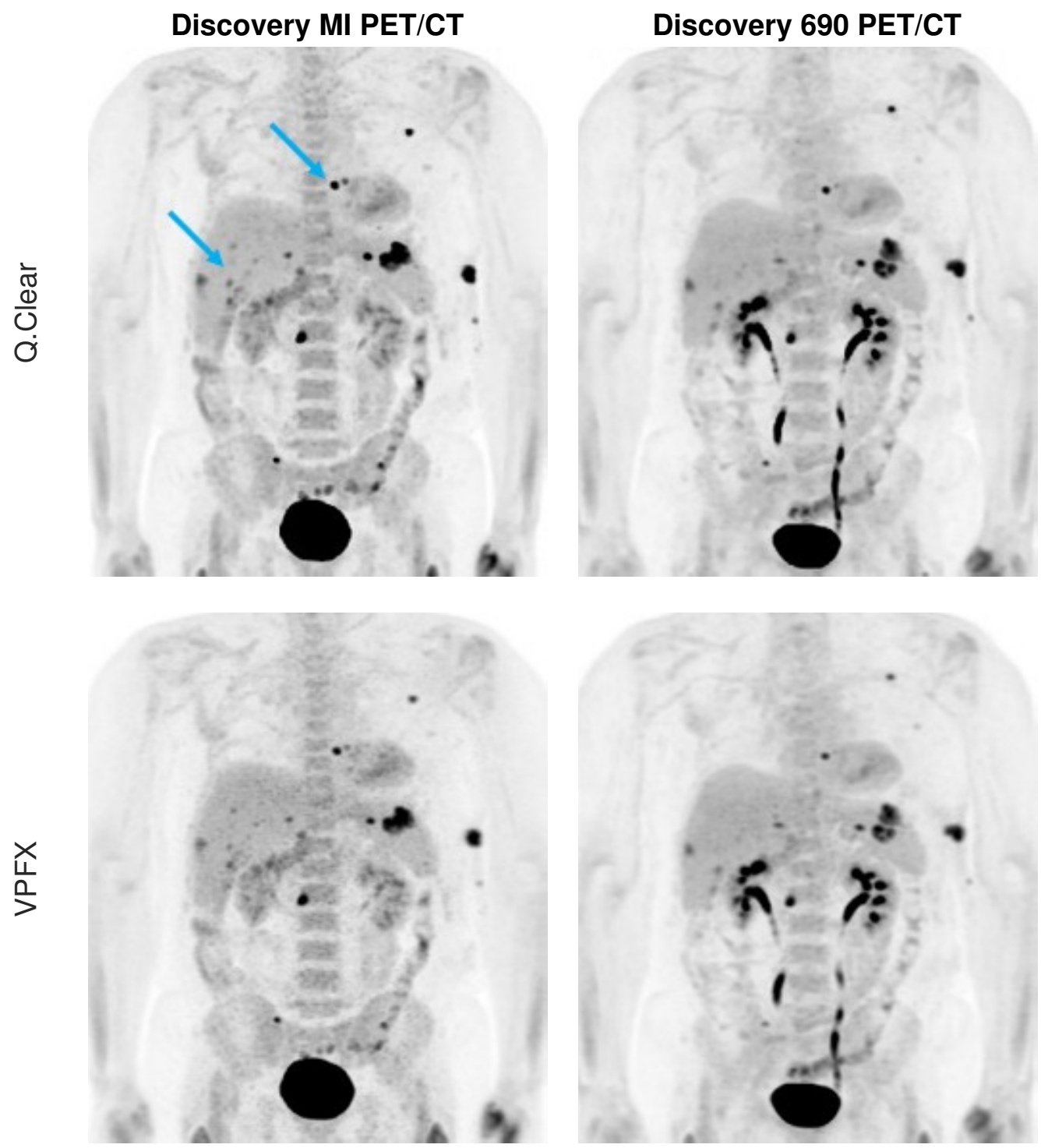

(a) Maximum-intensity projection coronal PET images.

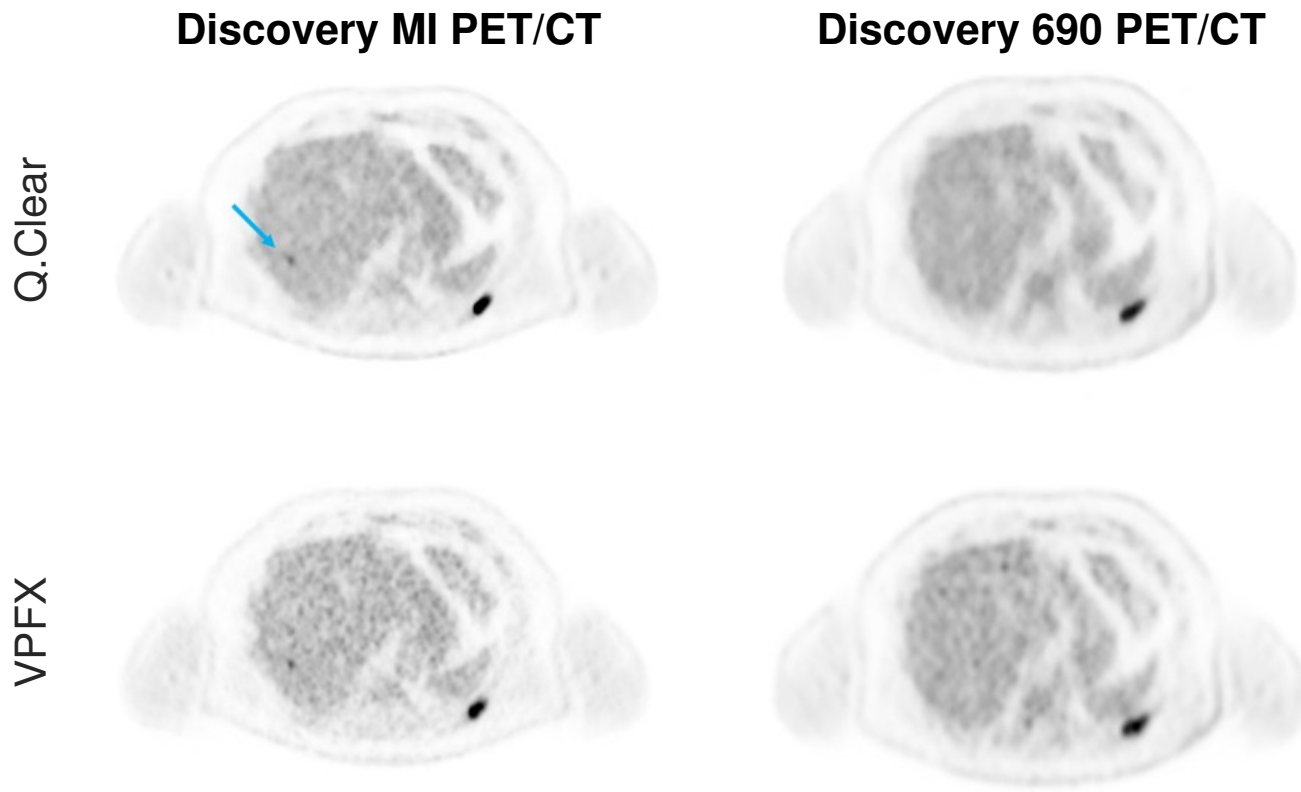

(b) Transaxial PET slices.

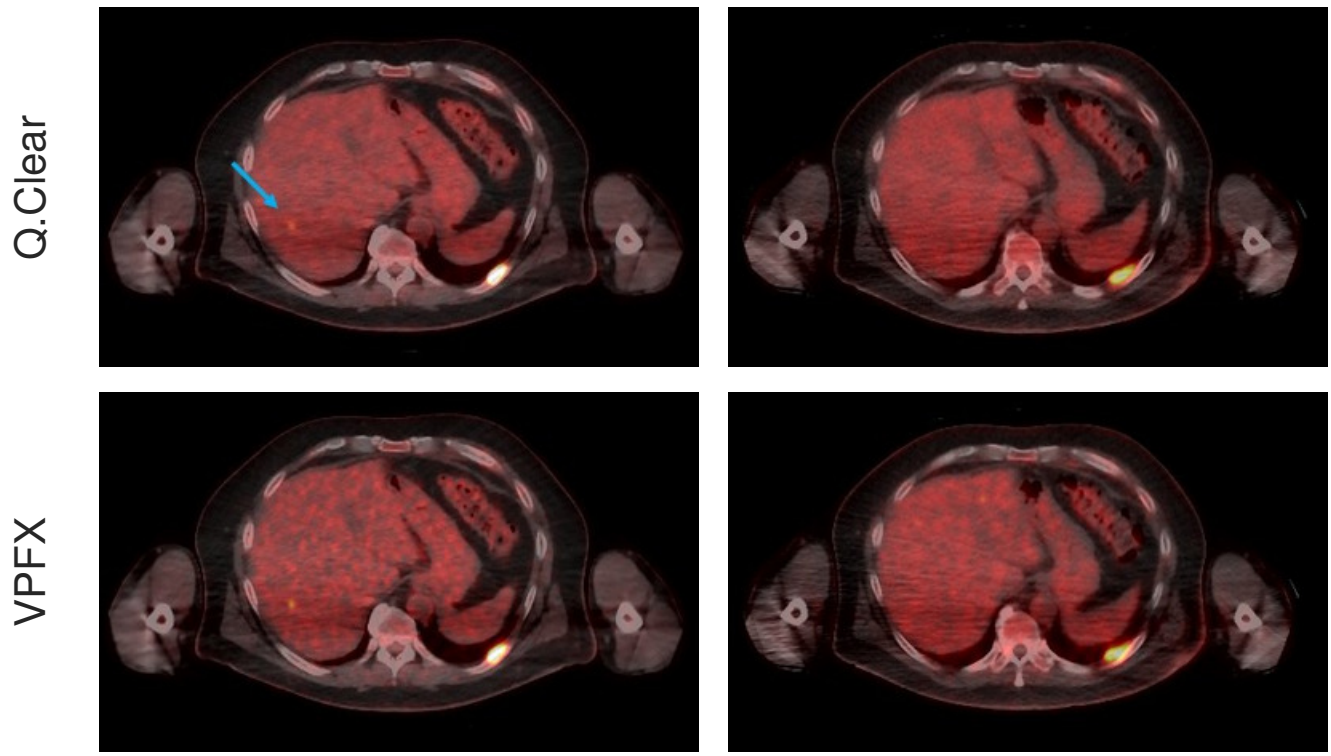

(c) Transaxial fused PET/CT images.

Figure 6: Melanoma patient scanned on both Discovery 690 and MI systems, reconstructed with VPFX and Q.Clear. The blue arrows indicate small metastases which are visible in the Discovery MI but not visible in the Discovery 690.

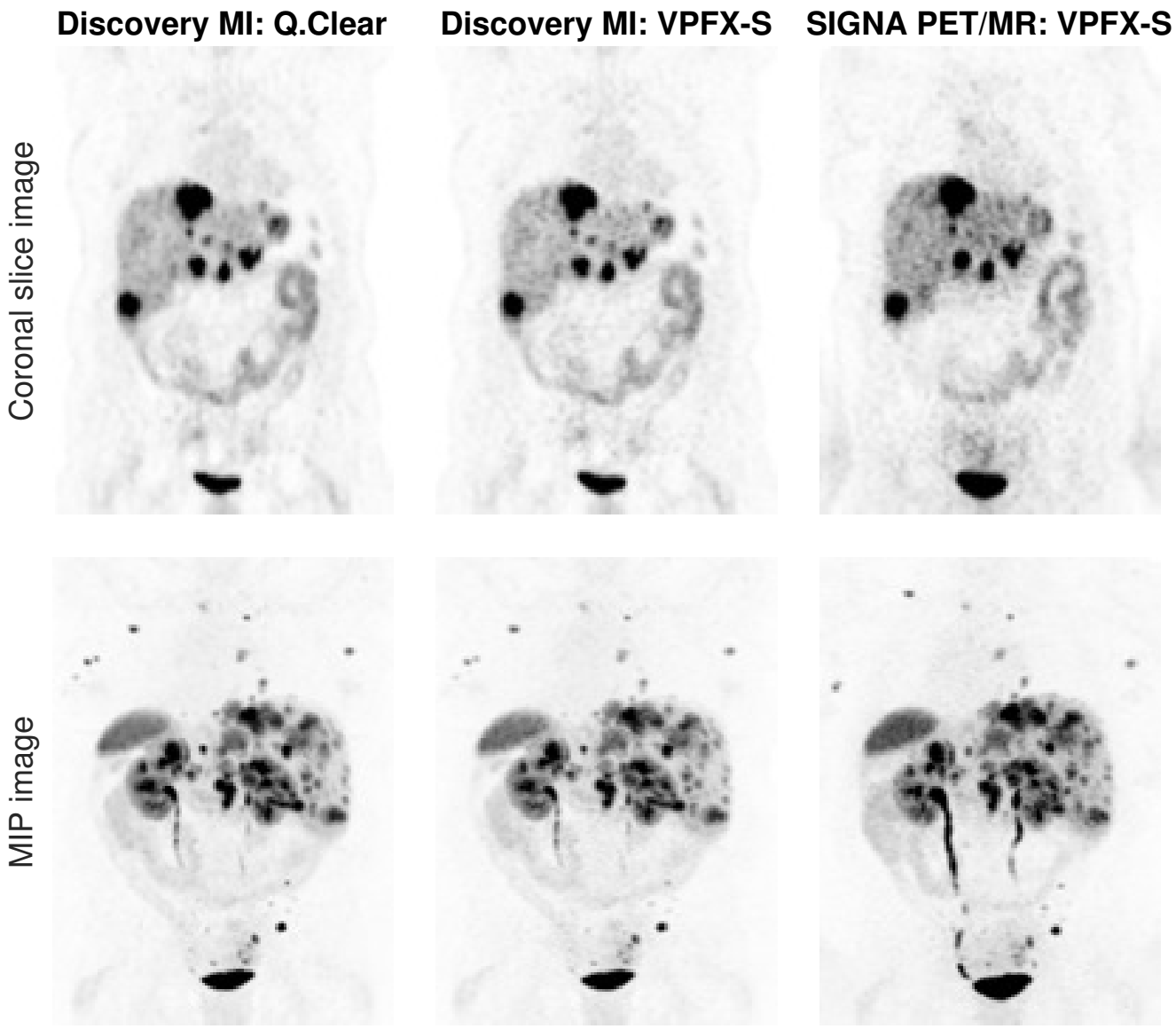

Figure 7: Reconstructed coronal slice and maximum-intensity projection images from the Discovery MI PET/CT (1st and 2nd column) and SIGNA PET/MR systems (3rd column). The second and third columns were reconstructed with the VPFX-S algorithm, while the first column was reconstructed with the Q.Clear algorithm.

Table 1: Image Reconstruction-Related Acronyms

Acronym	Reconstruction Algorithm
FBP	Filtered backprojection
OSEM	Ordered-subset expectation maximization
PSF	Point-spread function
VPHD	Non-TOF-OSEM without PSF modeling
VPFX	TOF-OSEM without PSF modeling
VPFX-S	TOF-OSEM with PSF modeling
Q.Clear	Block-sequential regularized expectation maximization with PSF modeling

Table 2: Spatial Resolution

Resolution Direction	**FBP Reconstruction**				**VPHD Reconstruction**			
	Stanford		*Uppsala*		*Stanford*		*Uppsala*	
	FWHM(mm)	FWTM(mm)	FWHM(mm)	FWTM(mm)	FWHM(mm)	FWTM(mm)	FWHM(mm)	FWTM(mm)
1 cm Radial Offset								
Radial	4.17	9.14	4.02	8.52	3.77	7.83	3.67	7.74
Tangential	4.40	9.17	3.97	8.19	4.00	7.95	3.74	7.93
Axial	4.57	10.38	4.39	10.12	4.00	9.80	3.93	9.71
10 cm Radial Offset								
Radial	5.65	10.36	5.28	9.95	4.76	9.08	4.68	9.11
Tangential	4.74	9.68	4.23	8.83	4.01	8.04	3.82	7.86
Axial	6.39	12.34	5.63	11.80	5.28	8.75	4.30	9.34
20 cm Radial Offset								
Radial	7.52	13.88	7.54	13.38	7.36	12.99	7.44	13.27
Tangential	5.13	10.14	4.67	9.04	4.62	9.03	4.31	8.46
Axial	6.50	13.01	5.70	12.57	4.09	9.71	4.01	9.75

Table 3: Count Rate Measurements

Measurement	Stanford	Uppsala
Peak NECR (kcps)	201.1	185.7
Activity at Peak NECR (kBq/mL)	22.1	21.7
Peak True Count Rate (kcps)	875.9	827.0
Activity at Peak True Count Rate (kBq/mL)	35.4	34.8
Scatter Fraction at Peak NECR (%)	40.4	40.8

Table 4: Contrast Recovery and Background Variability

Sphere diameter (mm)	VPFX Recon		Q.Clear Recon	
	CR (%)	BV (%)	CR (%)	BV (%)
Stanford				
10	51.7±2.3	10.2±1.3	67.2±5.1	7.9±0.7
13	61.5±6.2	7.8±0.7	72.5±4.4	6.2±0.4
17	66.2±2.0	6.0±0.2	74.4±0.8	4.8±0.1
22	81.3±2.1	4.8±0.2	87.7±0.8	3.8±0.4
28	86.6±1.8	3.8±0.1	91.1±0.6	2.9±0.3
37	90.0±1.4	3.0±0.2	94.0±0.5	2.4±0.3
Uppsala				
10	55.6 ±1.5	10.6±0.1	72.9±2.7	8.5±1.0
13	66.5±2.6	8.1±0.3	80.2±2.9	6.3±0.4
17	80.1±3.8	5.8±0.3	87.1±2.6	4.7±0.1
22	84.1±2.6	4.3±0.5	90.8±1.3	3.7±0.3
28	86.9±1.9	3.7±0.4	91.8±0.8	3.0±0.4
37	91.4±0.4	2.9±0.3	94.5±0.3	2.5±0.3

NEMA NU-2 Measurement	GE Discovery MI PET/CT (this work)	GE SIGNA PET/MR (12)	GE Discovery 690/710 PET/CT (4)‡	Siemens Biograph mCT Flow PET/CT (7)	Siemens Biograph mMR PET/MR (14)	Philips Vereos Digital PET/CT (20)§	Philips Ingenuity TF 128 PET/CT (8)
Axial FOV (cm)	20	25	15.7	22.1	25.8	16.4	18
Transverse FOV (cm)	70	60	70	70	59.4	67.6	67.6
Detector Ring Diameter (cm)	74.4	62.4	81.0	84.2	65.6	76.4	90
Crystal Thickness (mm)	25	25	25	20	20	19	22
Spatial Resolution FWHM, FBP Reconstruction							
Radial, 1cm	4.10	4.46	4.70*	4.33*	4.3*	4.01*	4.84*
Tangential, 1cm	4.19	4.08	4.70*	4.33*	4.3*	4.01*	4.84*
Axial, 1cm	4.48	5.35	4.74	4.25	4.3	4.14	4.73
Radial, 10cm	5.47	5.81	5.34	5.16	5.2	NA	5.25
Tangential, 10cm	4.49	4.44	4.79	4.72	4.8	NA	5.01
Axial, 10cm	6.01	6.75	5.55	5.85	6.6	NA	5.23
Radial, 20cm	7.53	8.42	NA	5.55	NA	5.82*	NA
Tangential, 20cm	4.90	5.27	NA	6.48	NA	5.82*	NA
Axial, 20cm	6.10	7.30	NA	7.80	NA	6.17	NA
Sensitivity							
Center of FOV (cps/kBq)	13.7 (7.5¶)	22.9	7.4	9.6 (5.4#)	15.0	5.7	7.39
Count Rate Statistics							
Peak NECR (kcps)	193.4	214.8	139.1	185	184	171	124.1
Peak NEC activity (kBq/mL)	21.9	17.6	29.0	29.0	23.1	50	20.3
Peak NEC Scatter fraction (%)	40.6	42.5	37	33.5	37.9	30	36.7
Accuracy of Corrections							
Maximum absolute error (%)	3.14	3.5	2.09	3.7	5.5	NA	NA
Image Quality, Measured Contrast Recovery in Spheres							
10 mm	53.7	36.5	44	28.5	32.5	62	17
13 mm	64.0	50.6	56	42.3	50.0	NA	46
17 mm	73.1	60.0	65	58.4	62.9	NA	58
22 mm	82.7	68.6	75	71.7	70.8	88	63
28 mm	86.8	80.7	87	70.1	65.1	86	68
37 mm	90.7	88.6	89	78.3	72.3	89	68
Timing and Energy Resolution							
Timing resolution (ps)	375.4	390	544.3	555†	2930	322	502
Energy resolution (%)	9.40	10.5	12.4	NA	14.5	11.0	11.1

Note: For each column, the numerical precisions listed are exactly as presented in that reference.
* Radial and tangential values are averaged together.
† Value is unclear in the reference.
‡ Discovery 690 and 710 systems have the same PET subsystem, so NEMA results apply to both.
§ Not yet commercially available.
¶ For Discovery MI system with 15 cm axial FOV (*16*).
# For Biograph mCT system with 16.2 cm axial FOV (*11*).

Table 5: NEMA NU-2 Measurements of other Commercial PET Scanners.